Author/s:
Doyle, SE;Duchi, S;Onofrillo, C;Quigley, A;Di Bella, C;Pirogova, E;O'Connell, CD

Title:
Printing between the Lines: Intricate Biomaterial Structures Fabricated via Negative Embodied Sacrificial Template 3D (NEST3D) Printing

Date:
2021-07-01

Citation:
Doyle, S. E., Duchi, S., Onofrillo, C., Quigley, A., Di Bella, C., Pirogova, E. & O'Connell, C. D. (2021). Printing between the Lines: Intricate Biomaterial Structures Fabricated via Negative Embodied Sacrificial Template 3D (NEST3D) Printing. Advanced Materials Technologies, 6 (7), https://doi.org/10.1002/admt.202100189.

# Printing between the lines: Intricate biomaterial structures fabricated via Negative Embodied Sacrificial Template 3D (NEST3D) Printing

*Stephanie E. Doyle, Serena Duchi, Carmine Onofrillo, Anita Quigley, Claudia Di Bella, Elena Pirogova, Cathal D. O'Connell**

S. E. Doyle, Dr. A. Quigley, Prof. E. Pirogova, Dr. C. D. O'Connell

Electrical and Biomedical Engineering, School of Engineering, RMIT University, Melbourne, Victoria 3000, Australia.

Email: cathal.o'connell2@rmit.edu.au

S. E. Doyle, Dr. S. Duchi, Dr. C. Onofrillo, Dr. A. Quigley, A/Prof. C. Di Bella, Dr. C. D. O'Connell

ACMD, St Vincent's Hospital Melbourne, Fitzroy, Victoria 3065, Australia.

Dr. S. Duchi, Dr. C. Onofrillo, A/Prof. C. Di Bella

Department of Surgery, The University of Melbourne, Fitzroy, Victoria 3065, Australia.

Dr. S. Duchi, Dr. C. Onofrillo,

ARC Centre of Excellence for Electromaterials Science, Intelligent Polymer Research Institute, University of Wollongong, Wollongong, NSW 2522 Australia.

Dr. A. Quigley



This is the author manuscript accepted for publication and has undergone full peer review but has not been through the copyediting, typesetting, pagination and proofreading process, which may lead to differences between this version and the Version of Record. Please cite this article as doi: 10.1002/admt.202100189.

Department of Medicine, The University of Melbourne, St Vincent's Hospital Melbourne, Fitzroy, VIC 3065, Australia.

A/Prof. C. Di Bella

Department of Orthopaedics, St Vincent's Hospital Melbourne, Victoria 3065, Australia.

Keywords: additive manufacturing, tissue engineering, biomaterials, degradable scaffolds, biofabrication



## 1. Abstract:

Extrusion printing techniques are widely used across tissue engineering and related fields for producing 3D structures from biocompatible thermoplastics, however the achievable structural complexity and porosity can be limited by the nozzle-based, layer-by-layer deposition process. Here we illustrate how this limitation can be overcome through a new technique termed Negative Embodied Sacrificial Template 3D printing. We demonstrate how the negative pattern within a 3D printed object can describe geometries that are not possible to extrusion print directly, and at definitively higher resolution. Negative patterns in a water-soluble sacrificial template can be 'developed' by casting in a secondary material and dissolving the template, creating exquisitely complex 3D structures including hyper-branched dendritic structures and open lattices with stiffnesses tuneable over 3 orders or magnitude. The technique is amenable to a plethora of materials from biodegradable thermoplastics (such as polycaprolactone) to resins (including acrylic and epoxy), silicones (including the Sylgard 184 polydimethylsiloxane formulation), ceramics

(including hydroxyapatite composites), hydrogels (including agarose and gelatin methacryloyl), low-melt temperature metal alloys and others. Using an unmodified, consumer-grade printer, NEST3D printing achieves high resolution, intricate biomaterial structures with potential applications in biomedical implants and tissue engineering scaffolds.

## 2. Introduction

Many fields of contemporary research, including tissue engineering, organ-on-a-chip and biomedical devices, are underpinned by technologies used to create three dimensional structures from biocompatible materials.[1] Light or energy-based fabrication techniques are typically favored for generating high-resolution, complex structures in largely unconstrained geometries.[2–5] However these techniques operate using highly specified chemistries and so materials typically require functionalization and careful tuning to be rendered processible

requirements that may have knock-on effects in terms of biomaterial function, and which may complicate the process of translation as medical devices.[84] Nozzle or extrusion-based 3D printing techniques (including direct ink writing, bioplotting and fused-filament fabrication/fused deposition modelling (FFF/FDM) are more widely applicable across materials classes, from polymers, [6,7] to hydrogels, [8] ceramics, [9] living cells [10] and beyond.[1] However the conventional process of layer-by-layer deposition can constrain the geometries these techniques can produce, since the deposited material must typically be physically supported by the existing structure or sacrificial supports.[11] While several extraordinary examples of free-form printing have been demonstrated,[14],[32][81-83]

these have so far only been demonstrated for certain classes of rapidly solidifying inks, and are yet to be extended more broadly to biomaterials such as hydrogels or degradable polymers of interest in tissue engineering. Embedded printing technologies can also overcome many of the constraints of nozzle-based deposition by printing into a support bath.[12,13] However these techniques have also not yet been demonstrated for biocompatible thermoplastics, which are the most widely used materials for generating degradable implants and tissue engineering scaffolds.

Another strategy, compatible with thermoplastics as well as many other classes of materials, is to first generate the supporting structure before adding the final material. In a family of techniques broadly termed 'indirect printing', the printer is used to create sacrificial templates which are filled with a secondary material, then dissolved or otherwise removed. While the sacrificial mold concept can be traced back to the 6000 year old metallurgical technique of 'lost-wax' or 'investment' casting,[15][16][17] modern iterations adapt computer aided design methods by 3D printing the sacrificial mold.[16,18] Indirect printing is attractive because it allows 3D structures to be created from castable materials which would be challenging to 3D print directly, such as silicones, ceramics and low viscosity hydrogels.[19–23] Through careful choice of materials and additives, casted structures can even be generated with higher resolution than the original mould.[19] So far, however, the structures created by indirect printing have been relatively simple log-pile or gyroid structures—all of which can be created by conventional extrusion printing.

Here, we introduce a new technique, Negative Embodied Sacrificial Template 3D (NEST3D) printing, which can be used to create highly intricate 3D geometries from biomaterial thermoplastics and other materials. NEST3D printing circumvents the constraints of extrusion printing by defining the pattern of the desired object in the 'negative' space between the printed lines. Because channels of

negative space can be arbitrarily stacked; the negative pattern within a 3D printed structure can describe geometries that would be extremely difficult, if not impossible, to extrusion print directly using biomaterials, even with the use of a support material. The negative pattern can then be developed by pressure casting a secondary material and dissolving the template. In this manner we demonstrate how an unmodified, consumer-grade FDM printer can create high-resolution 3D objects with arbitrarily oriented structural elements. This capability allows us to generate degradable scaffolds for tissue engineering with stiffness tunable over three orders of magnitude and porosities of up to 97%.

## 3. Results and Discussion

Our central hypothesis is that that the negative pattern within a 3D printed object can be defined with greater structural freedom and resolution than the printed object itself, and that such a pattern can be used to cast complex 3D structures from a broad range of functional materials. To evaluate this idea, we first focused on developing a system for fabricating negative patterns within a suitable sacrificial template.

Sacrificial templates have previously been created using FDM printed Acrylonitrile butadiene styrene (ABS) or polyvinyl alcohol (PVA), extrusion printed Pluronic hydrogels, and using Selective Laser Sintering (SLS) printed carbohydrate glass.[2,19–21] We chose the polymer PVA as our sacrificial material because it is water-soluble, amenable to the widely accessible FDM technique, and because we expected the printed templates to be rigid enough to cast a range of high viscosity materials. In early experiments we optimized the printing settings on a consumer grade FDM printer to maximize

resolution of the spacing between the printed lines, as well as the material preparation and storage protocols needed to achieve consistent and high resolution PVA printing (see Methods). In these experiments we measured the width of extruded PVA fibers to be 350-400 $\mu$m depending on the settings but found that the spacing between the lines could be as low as ~100 $\mu$m across. We took this as a preliminary proof of our concept, and a potential target for a castable resolution.

We next developed the basic strategy to 3D print the negative pattern within a standardized cuboidal template, including inlet holes (for the casted material) and outlet holes (to allow trapped air to escape). We chose the degradable polymer polycaprolactone (PCL) as our model material as it is one of the most widely applied polymers in biomedical engineering today, being in clinical use in sutures, drug delivery, as well as being a prominent choice in tissue engineering scaffolds.[24] While PCL is sometimes processed as a solution in chloroform, we opted for a solvent free approach to avoid any possibility of residual solvent in the final product. Thus, casting PCL required heating it to above its melting temperature (60 °C) where it formed a viscous (>1000 Pa·s) liquid. We explored several methods of filling these templates with molten PCL, including drop (i.e. gravity driven) casting, centrifugation and pressure-casting. Gravity alone was not enough of a driving force to fill the template with molten PCL even after overnight in the oven, and centrifugation tended to warp the PVA molds, unavoidably distorting the pattern inside. We found pressure-driven casting to be most successful filling method and developed a simple pneumatic system which can be assembled using commonly available lab consumables (Figure S1).

Finally, we developed a software workflow to create the 3D design file and invert it into a castable template. Our final NEST3D printing workflow is illustrated in Figure 1(A-E). In this process we first use CAD software to design the desired 3D structure (Figure 1A). We then digitally invert this model to form the cavity image within a solid template called the NEST. We use a consumer-grade FDM printer to 3D print the NEST in PVA (Figure 1B). We load the 3D printed template into a custom-built chamber and use pneumatic pressure to force a secondary material into it, completely filling the negative pattern (Figure 1C). We then remove the template from the chamber and place it in water to dissolve (Figure 1D). Once all of the PVA dissolves, the secondary material is revealed in the desired 3D structure (Figure 1E). As a sequential X-ray microtomography (micro-CT) analysis shows, the complex geometry of the original CAD model (Figure 1F) is recapitulated in the negative space within the NEST (Figure 1G), and in the final casted structure (Figure 1H).

NEST3D printing is essentially a marriage of additive fabrication and injection moulding, and it overcomes several limitations inherent in each technique. We discuss throughout this paper how NEST3D can outperform direct extrusion printing in certain aspects of fabricable complexity, porosity and contiguity. Injection moulding is ubiquitous in mass manufacturing of plastics, and has also become attractive for small batch production due to the emergence of 3D printed molds.[25] Neverthless, injection moulding can only be used to make relatively simple structures, without internal complexity. This is because the molds are created in two parts which must be pulled apart to remove the casted object. Our methodology differs in that we inject material into a mould which is sacrificial, allowing us to generate far more complex architectures than are achievable with a two-part mold.

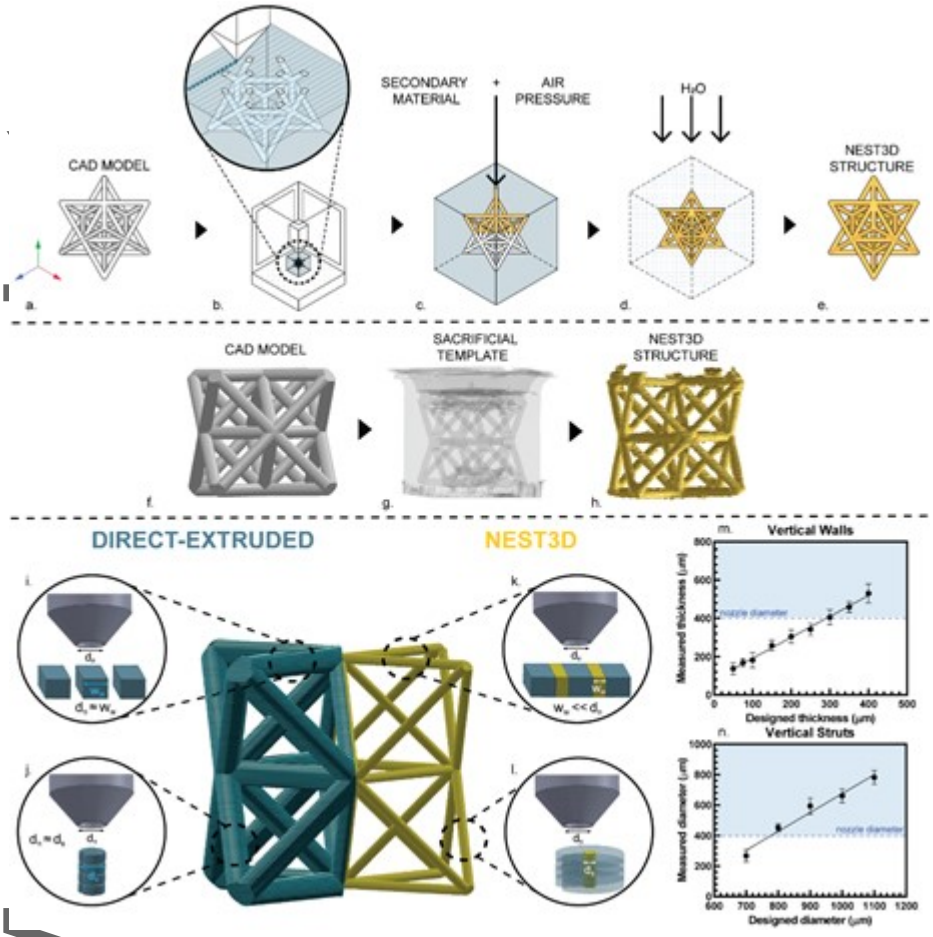


***Figure 1 | NEST3D printing concept.*** *(**A-E**),* *NEST3D printing process: (**A**).* *CAD model is designed. (**B**) The CAD model is digitally inverted to create the sacrificial template. The sacrificial template is then FDM printed whereby the original design (**A**) is patterned in negative (empty) space. (**C**) The negative space is filled with the secondary material with the assistance of air pressure. (**D**) After the casted material is set (i.e. via gelation, solidification, or crosslinking etc.) the sacrificial template is dissolved in water. (**E**) The final structure is composed of the casted material, is fully contiguous and matches the desired structure in (**A**). (**F-H**) NEST3D printing fabrication steps shown with micro-CT reconstruction. (**F**) CAD model. (**G**) micro-CT scan of the unfilled sacrificial template. (**H**) micro-CT scan of a NEST3D printed PCL structure created after the template in (**G**) was filled and dissolved. (**I-L**) A comparison of 'direct-extruded' 3D printing with the NEST3D printing strategy. (**I-J**) In direct extrusion-based 3D printing, the minimum achievable strut width is approximately equal to that of the nozzle diameter; (**K-L**) In NEST3D printing, the resolution is determined by the spacing between deposited lines. (**M**), The*

*minimum feature sizes achieved using NEST3D printing (140 µm) is less than half that of the nozzle diameter. (**N**), NEST3D printing resolution for vertical struts composed of PCL was 270 µm, which again is less than the nozzle diameter.*



**NEST3D printing unlocks sub-nozzle resolution**

After developing our NEST3D printing workflow, we turned to the question of feature resolution. With unmodified, consumer-grade FFF/FDM extrusion printers, the minimum feature sizes achievable of thermoplastics is typically similar to the nozzle aperture.[26,27] While high resolutions can be achieved by employing ultra-fine nozzles [28,29], or through electrohydrodynamic jetting techniques [30], scaling these methods up beyond the millimeter scale remains a major challenge. The potential for NEST3D printing to break through the nozzle aperture constraint hinges upon the idea that the negative spacing between two 3D printed lines can be arbitrarily narrow (Figure 1K). In fact, using our system we routinely cast vertical PCL features with widths less than half that of the nozzle (Figure 1M). Our minimum vertical wall thickness is approximately 140 $\mu$m when a 400 $\mu$m aperture nozzle was used. The measured thickness of vertical PCL features created using NEST3D printing is typically a little higher than that defined by the original CAD design, but this deviation is well fitted by a linear trendline ($y$ =1.09$x$+82 $\mu$m, with $R^2$ = 0.996) and so can be calibrated for in the design stage. Using a 60 $\mu$m stepping resolution, NEST3D printing can produce horizontal structural elements with a cross-section of approximately 140 $\mu$m x 60 $\mu$m. Even smaller dimensions may be achievable by using finer nozzle apertures.

**NEST3D printing enables the construction of high-resolution vertical struts**

Conventional nozzle-based 3D printing techniques are suited to depositing stacked horizontal lines, but not free-standing vertical features. Attempts to directly print such structures using our FDM printer resulted in irregular structures replete with blobbing and stringing defects, even when a dual-nozzle system with soluble support was used (Figure S2). Direct extrusion of vertical struts (Figure 1J) requires a delicate balance of process parameters such as flow rate, movement velocity and thermal control[14],[32][81-83] and has not yet been achieved for thermoplastic biomaterials such as PCL. On the contrary, vertical cylindrical cavities can be easily created by stacking ring-shaped extrusion profiles (Figure 1L). Thus, NEST3D printing enables the facile fabrication of vertical (or arbitrarily angled) cylindrical struts. Using polycaprolactone as a model material, we have created vertical struts with diameters as fine as 270 µm, again utilizing a 400 $\mu$m aperture FDM nozzle (Figure 1N). These struts are fully contiguous structures, with no internal defects due to interlayer bonding as prevalent in conventional 3D printing technique.[33–35] In the mechanical testing section below, we show how lattice geometries created using this approach can achieve a broad range of stiffnesses while maximizing porosity.

**The template filling time can be modelled analytically**

In preliminary experiments, we pressure-casted the material for 1 hour, but noticed that this was not always adequate to completely fill the higher resolution templates. This prompted us to examine the pressure-casting process. We hypothesized that the filling process in our pressure driven casting system follows conventional expressions for the flow in a pipe:

$$Q = \frac{\pi r^4 \Delta P}{8\eta L} \quad (1)$$

where $Q$ is flow rate, $\eta$ is the viscosity of the secondary material, $L$ is the length, $P$ is the pressure differential between the inlet and outlet points and $r$ is the radius of the cylinder. [36,37] Integrating yields an expression for the volume filled as a function of time (t) in seconds:

$$V(t) = \sqrt{\frac{\Delta P t}{4\,\eta}}\pi r^3 \quad (2)$$

We tested this model by measuring the time to fill individual cylindrical cavities. We fabricated NESTs incorporating long cylindrical cavities with diameters ranging from 800 $\mu$m to 1200 $\mu$m, and pressure-casted PCL into them using a range of filling times (from 60 seconds to 50 minutes). The experiments were repeated using two grades of PCL with different viscosities (110 and 1100 Pa·s). Our empirical data generated from dozens of individual experimental runs shows excellent agreement with the model predictions (Figure 2A). A similar discussion for filling of thin walls (rather than cylinders) is included in the supplementary information (Figure S3). In essence, this model allows for estimating the filling time required for templates with different feature sizes and/or for materials of different viscosities. Whilst we have only validated these models with PCL materials, the treatment should be directly applicable to other newtonian liquids. Non-newtonian liquids however would require more complicated expressions which incorporate shear-thinning or shear-thickening behaviour.

**Template dissolution can be accelerated using ultrasonication compared to gentle shaking**

Following the casting step, the sacrificial template is dissolved in water. To quantify the PVA dissolution over time, we monitored the dissolution process via Fourier-transform infrared (FTIR)

spectroscopy performed on aliquots of the water solution at sequential time-points. A 1 $cm^3$ sacrificial template can be entirely dissolved (i.e. where no detectable traces of PVA remain in the soaking solution) in an ultrasonic bath within 5 hours (Figure 2B). Fragile materials (such as hydrogels), which may be damaged by sonication, can instead be developed by dissolving the PVA on an incubator-shaker at 37 °C for 3 days (Figure S4).

**NEST3D printing produces cytocompatible 3D biomaterial structures**

With our target applications primarily being in the tissue engineering field, we next assessed whether 3D structures prepared using NEST3D printing would leach residual PVA that might be potentially cytotoxic towards human stem cells. While PVA is widely used as a biomaterial, we cannot exclude the possibility that our commercially bought PVA filament contains other additives which may negatively impact cell viability. Thus we designed an experiment to detect any potential cytotoxic effect of residual/trace PVA released/leached out in our NEST3D scaffolds once maintained in standard cell culture media in a cell incubator environment.[38]

In these experiments, we chose to probe the viability of human mesenchymal stem cells (hMSCs) owing to their wide applicability in tissue engineering and clinical translation studies.[39] We prepared PCL NEST structures which were dissolved and cleaned following the ultrasonication dissolution protocol. Once prepared and cleaned, samples were soaked in cell culture media for one week to generate the conditioned media. The cell population did not show any decrease in metabolic activity over 24 hours of culture with respect to a control group in fresh cell medium or compared to conditioned media from PCL log-piles made via FDM printing (GeSim BioScaffolder 3.2, GeSiM,

Radeberg, Germany) (Figure 2C). The fact that cell viability was not significantly attests to the benign nature of the NEST3D printing process in terms of removal of potential toxic components from the PVA sacrificial material.

**NEST3D printing can be used to generate highly complex 3D biomaterial structures**

Fabrication techniques based on layer-by-layer deposition of material are generally constrained in terms of the achievable complexity of the printed microarchitecture.[4,40] By building a pattern in negative space, our technique circumvents these conventional limitations, allowing us to generate structures with any combination of vertical, horizontal or angled structural elements (Figure 2D-K). The examples shown illustrate our ability to create highly porous structures with <5% volume fraction of PCL (Fig 2J). Highly porous scaffolds are particularly important in tissue engineering for allowing cell infiltration, matrix deposition and vascularization.[41] Even more exotic structures can be created using NESDT3D printing, such as the hyper-branched tree-like model in Figure 2L. Dendritic structures are notoriously challenging to fabricate with 3D printing as they are contain many unsupported overhangs and underhangs as well as load-bearing branches oriented obliquely to the x, y and z axes.[2] The NEST3D tree model measures over 80 mm tall, and yet is composed of individual, self-supporting branches which are as fine as 800 $\mu$m. This is an example of complex fabrication at hierarchal scales rivalling that which is achievable with biomaterials using light-based fabrication.[2] Figure 2M shows a 3D Voronoi lattice of an ear model in PCL with individual struts of 800-900 $\mu$m. This structure is highly porous (>90% empty space) and is a highly curved model

tracking the contours of a human ear, and would be extremely difficult to extrusion print directly, especially in PCL.

NEST3D printing also allows the creation of smooth structures without the characteristic ribbed surface of conventional 3D printed parts. While our NESTs are nominally imprinted with such a ribbed surface after emerging from the FDM printer (Figure 2N) this ribbing can be smoothed by simply flushing the template with water prior to filling it with the secondary material. Structures subsequently casted from water-flushed NESTs have a smooth outer surface (Figure 2O), as well as being internally contiguous. For struts made with a sacrificial template of 0.06 mm layer height (Figure 2N), the edge roughness of an untreated strut is 59.58 ± 30.39 $\mu$m, however after being treated with water (Figure 2O) the roughness reduces to 22.17 ± 7.65 $\mu$m. Further details can be found in Figure S5.

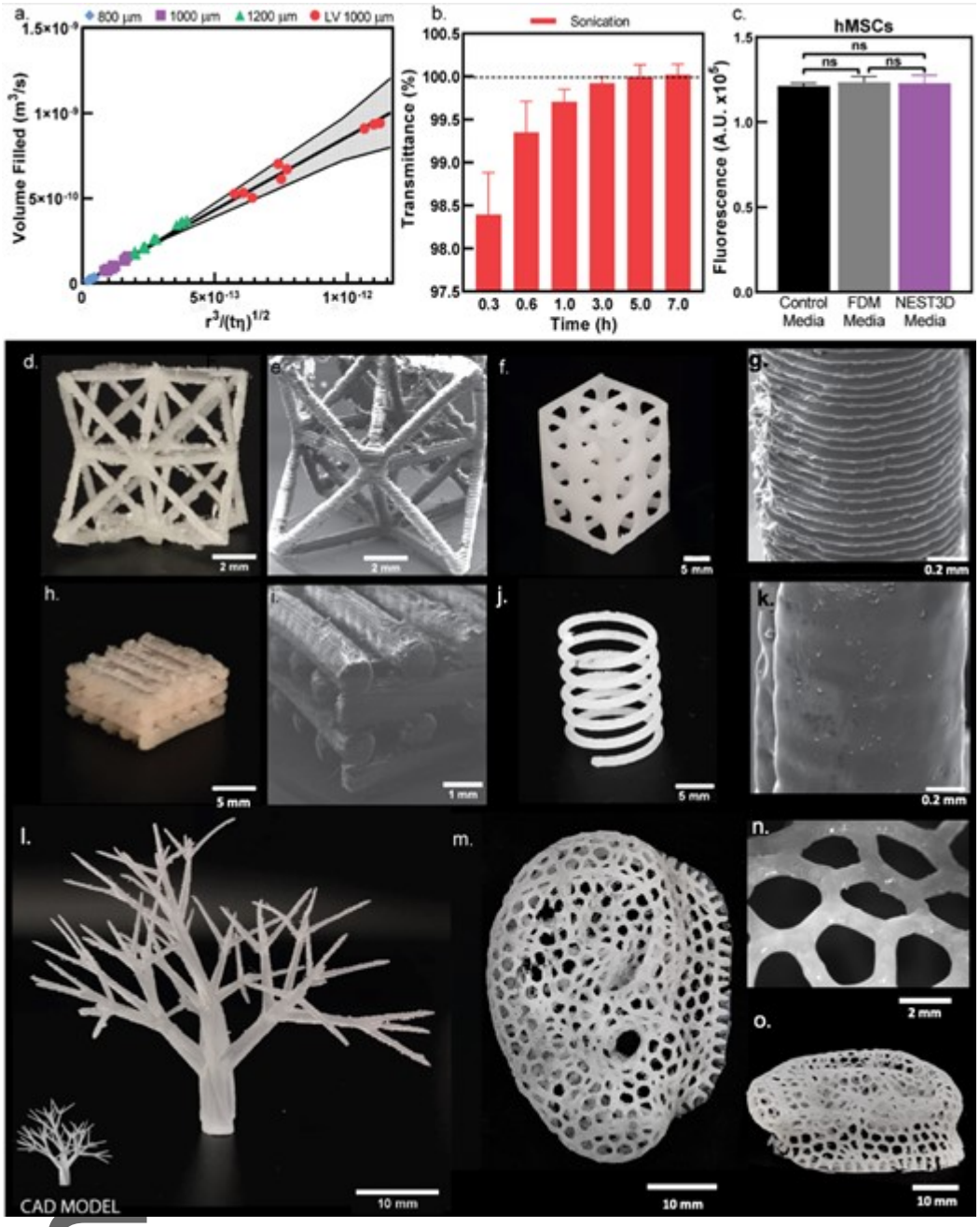


**Figure 2 | Fabrication characteristics and design complexity of NEST3D printing. (A) Predicted (solid line) and empirically measured (data points) flow rates for the filling of individual cylindrical struts within the sacrificial template. To validate the model described by equation (2), volume flow rate should be linear with respect to $r^3/(t\eta)^{1/2}$. This plot includes data for three strut diameters (800, 1000 and 1200 µm) filled using PCL with a**

**viscosity of 1100 Pa·s. and 1,000 µm diameter struts filled with PCL with a viscosity of 110 Pa·s (LV=low viscosity). The shaded region shows the standard deviation of the predicted model. (B), FTIR measurements of the water used to dissolve the sacrificial PVA template as a function of ultrasonication time. A measurement of 100% transmittance with respect to the blank reference solution was achieved after 5 hours of sonication, indicating the complete removal of PVA below the detectable limit. (C) A cell viability assay showed no detectable cytotoxicity, to hMSCs of leachate from PCL NEST generated lattices after 7 days of leaching. This is when compared to both regular culture media and leached media from FDM generated PCL lattices. (D-J) A showcase of achievable design complexity, all produced in PCL; All images are photographs, excluding E and I which are SEM micrographs. (G) SEM micrograph of a PCL vertical strut fabricated by NEST3D printing using an FDM layer height of 0.06 mm. (O) SEM micrograph of a PCL vertical strut generated after the 0.06 mm template (as in (G)) was flushed with water to smoothen the surface. (L) Large scale tree model created in a clear casting resin. Tree measures approximately 85 mm tall with varied sized branches from approximately 10 mm at the trunk to under 1 mm at the outermost branches. (M) Human scale ear lattice (polycaprolactone) measuring approximately 6 mm long and 4.5 mm wide with struts between 0.8-0.9 mm diameter. (N) Stereomicroscope image showing detail of the fully contiguous Voronoi lattice used to define the outer surface of the ear scaffold. (O) Side on view (photograph) of the ear scaffold shown in M, illustrating its height and the requirement for several overhangs which would make this structure a challenge to produce using PCL by direct extrusion.**

## NEST3D printing can produce PCL geometries which cover a wide and clinically relevant range of porosity and stiffness

In tissue engineering and implant design, stiffness mismatch between the implant and natural tissue can lead to implant failure.[42–44] Due to the aforementioned constraints of layer-by-layer fabrication, extrusion-based 3D printing techniques of thermoplastic materials using unmodified, consumer grade printers, typically produce structures composed of stacked horizontal struts, such as the classic ‘log-pile’ pattern, where sequential layers of deposited lines alternate by a 90° rotation.

Embedded extrusion processes circumvent this limitation but so far are not amendable which thermoplastic materials. The mechanical properties of log-piles are tunable by controlling the volume-fraction (porosity) of the structure, and can be modulated to a lesser extent by the filling pattern and offset.[45,46] However, far greater mechanical tunability is theoretically achievable with cellular lattice structures which maximise properties such as stiffness to weight ratio.[47–51] Owing to the challenge of fabricating such designs in relevant biomaterials, these intricate geometries remain largely unexplored in tissue engineering and related fields.

Using PCL as an example material, we have produced lattice structures which attain stiffnesses across three orders of magnitude, from below 10 kPa to over 10,000 kPa (Figure 3). This stiffness range is driven by both the increased design complexity achievable by NEST3D printing and our ability to tune the strut diameters (Figure 3A). This range of stiffness encompasses a range of tissues which are targets of tissue engineering approaches, from breast tissue to articular and auricular cartilages (Figure 3B). The range of stiffnesses and porosities reported here is unprecedented for one single biomaterial, covering a broader range than has been reported in the same material by other techniques, including melt electrowriting (MEW), FDM and SLS (Figure 3C).

3D printed structures typically display anisotropic mechanical properties due to structural weaknesses inherent in layer-by-layer manufacturing.[33–35] By contrast, NEST3D printing produces final parts which are internally contiguous and the mechanical behavior of these structures can be accurately predicted using only intrinsic, bulk material properties (i.e. Young's modulus) without consideration of layer thickness, raster angle, interlayer bonding etc. Finite element analysis (FEA)

simulations of our NEST structures under compression predict stiffnesses in excellent agreement with our empirical measurements, especially for stiffnesses above 500 kPa (Figure 3D). Although the agreement is somewhat poorer for softer structures which include angled hinge points, likely due to a sensitivity to slight deviations in strut thickness at the point of bending. The remarkable agreement between simulation and experimental results attests to the broad applicability of the NEST3D printing technique to be used in computationally aided design approaches such as generative design or topology optimization for rational design and manufacturing of patient specific implants.[42,52]

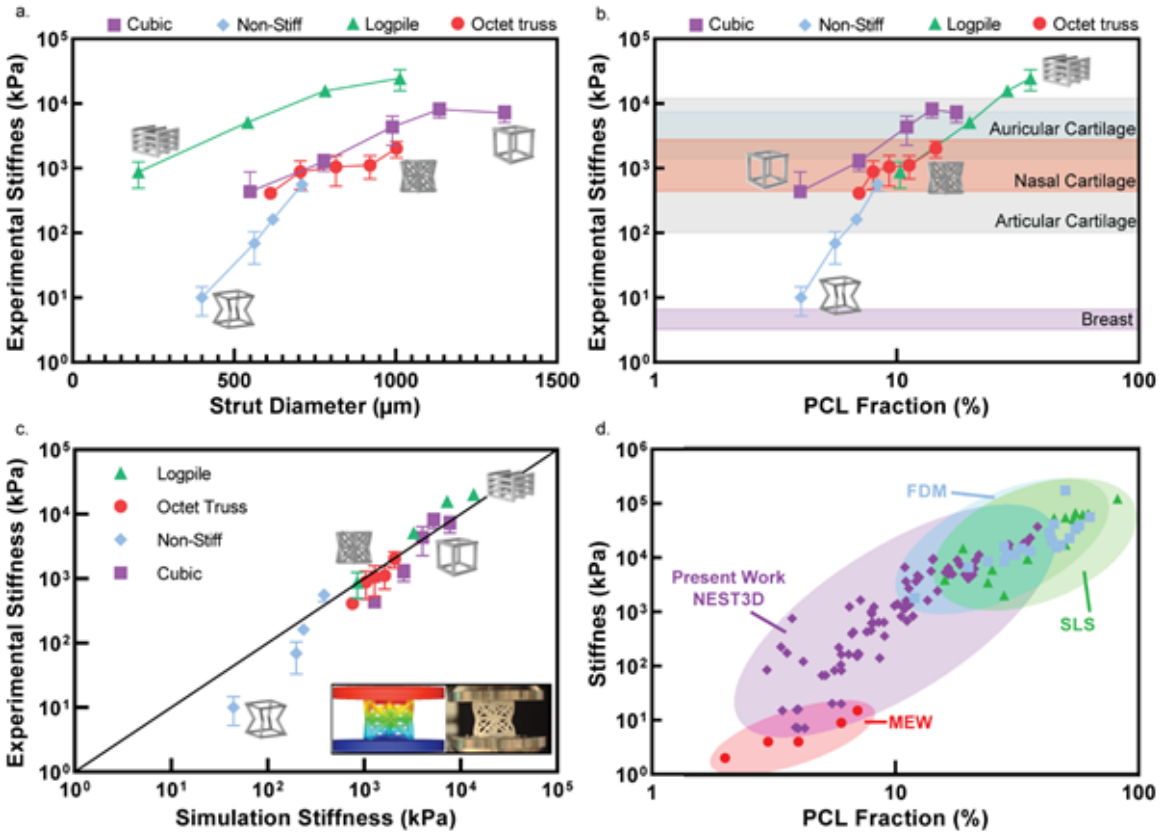


**Figure 3 | High degree of mechanical tunability afforded by NEST3D printing. (A) The compressive stiffness of PCL structures can be controlled across more than three orders of magnitude by modulating lattice design and strut diameter. (B) The achievable window of mechanical properties encompasses a range of body tissues**

**which are active targets of research in tissue engineering, including breast tissue, articular cartilage, nasal cartilage and auricular cartilage. (C) NEST3D printing can achieve an unprecedented range of stiffnesses and porosities using PCL when compared to literature data from Fused Deposition Modelling (FDM), melt electrospinning writing (MEW) and selective laser sintering (SLS).[53–61] (D) FEA simulations of NEST structures under compression show excellent agreement with empirical values, especially for stiffnesses above 500 kPa.**

**NEST3D printing can be applied to a wide range of material classes**

Over 50 3D printing technologies were recognized by the International Organization for Standardization in 2015, however most of these individual techniques are compatible with just one class of material, such as thermopolymers for FDM and photocrosslinkable materials for SLA, digital light processing, etc.[62] (Figure S6). Vast resources are expended in developing materials libraries amenable to each technique, which encompass a range of target properties such as elasticity, hardness and stiffness required for different applications. These formulations are typically not cross compatible between 3D printing techniques.

In developing a new material, compromises are often made to satisfy the conditions of processing at the expense of the target functionality. Rendering a material processible via light based fabrication techniques requires photoactive functional groups, and such functionalization unavoidably changes the properties of the original material, triggering the requirement for extra characterization, validation and/or regulatory approval steps.[63] 3D extrusion printing techniques are less constrained in terms of chemistry, but still generally favor materials which can undergo rapid phase change and are much less applicable to slow-setting materials such as epoxy and silicone resins. Tight processing windows mean that developing any new materials for 3D printing is highly time-consuming, typically involving laborious printing optimization processes.[13] Studies optimizing the extrusion printing of

PCL alone have examined the effects of temperature and viscosity, extrusion pressure, layer height, nozzle diameter, nozzle movement speed, turning angle, heat flow and shear stress among many others.[26,27,64,65]

By contrast, the NEST3D printing technique is versatile across a wide range of material classes including biomaterial polymers and polymer-ceramic composites, hydrogels, low melt-temperature metal alloys as well as slow-setting silicone elastomers and various resins (Figure 4A-J). The epoxy resin (Figure 4A) is an off-the-shelf craft products and is just one of many thousands of castable materials which can potentially be NEST3D printed without modification. Any material with the potential to solidify in a water-insoluble form is potentially NEST3D printable, such as a simple mixture of wood flour and glue (Figure 4B). The Sylgard 184 formulation of polydimethylsiloxane (PDMS) demonstrated in Figure 4H is one of the most widely used materials in biomedical engineering today, with applications across microfluidics, cell culture substrates, flexible electronics, and medical devices, and yet has been highly challenging to fabricate using 3D printing owing to its long setting times. Routine 3D fabrication of PDMS structures could open up many applications in non-planar microfluidics and 3D cell culture systems, as does the ability to form complex structures from castable hydrogels such as agarose (Figure 4J and Figure S7) and GelMa (Figure 4I). Field's alloy is a low melt metal that has been used to make electrodes for interfacing with living cells (Figure 4C). Polycaprolactone (Figure 2E) can be mixed with nanoparticles of hydroxyapatite (HA), a mineral found in bone, to form composites with more than 20% ceramic content (Figure 4F), with huge potential in bone tissue engineering owing to HA's osteoinductive properties.[66] Materials already developed for different 3D printing techniques can be readily adapted to our system, including commercial resins developed for stereolithography (Figure 4G) and inks developed for polyjet 3D

printing (Figure 4D). Generating this array of structures requires neither additional optimization of printing parameters nor the filling technique. The choice of material also had little or no impact upon the achievable resolution or design complexity as previously described.

Some constraints around material castability are imposed by the PVA sacrificial template material. The Vicat softening temperature of PVA is approximately 60 °C.[67] High viscosity materials casted above this temperature have the potential to cause some deformation of the sacrificial template (Figure S8). Low viscosity materials can be casted at the temperatures up to approximately 110 °C (at which the PVA begins to oxidize). Another requirement is material stability in a slightly acidic environment (as low as pH 5) generated during the PVA dissolution step.[68] Using a pH buffer in the PVA dissolution step can ameliorate this. In our experience, most materials which are castable at moderate temperatures and insoluble in water once set (i.e. solidified, crosslinked or gelled) are amenable to the NEST3D printing process (Table 1).

**Table 1.** Materials and their parameters used with NEST3D printing.

| Material | Class | Setting mechanism | Casting Temperature (°C) | Setting time | Viscosity (Pa·s) | Solvent |
|---|---|---|---|---|---|---|
| Polycaprolactone | Thermoplastic | Thermal | 70 | minutes | 40- | Water |

| | | | | | | |
|---|---|---|---|---|---|---|
| | polymer | | | | 50,000 | |
| Polycaprolactone/ Hydroxyapatite | Thermoplastic polymer/ ceramic composite | Thermal | 70 | minutes | 50-85,000 | Water |
| PDMS | Silicone Elastomer | Covalent crosslinking | 23 | 1 hour | < 110 [69] | Water |
| Epoxy resin | Acrylic resin | Covalent crosslinking | 23 | 1 hour | < 0.6 [70] | Water |
| Acrylic resin for Stereolithography* | Acrylic resin | Free radical polymerization | 23 | 1 hour | ≤ 5 [71] | Water |
| MED610 Polyjet resin* | Acrylic resin | Free radical polymerization | 23 | 1 hour | - | Water |
| Field's alloy | Low melt-temperature metal | Thermal | 70 | minutes | 0.01-0.18 [72] | Water |
| Agarose | Hydrogel | Thermal gelation | 70-90 | 1 hour | 0-6 [73] | Phosphate buffer solution |

* With addition of 0.1-1% Azobisisobutyronitrile

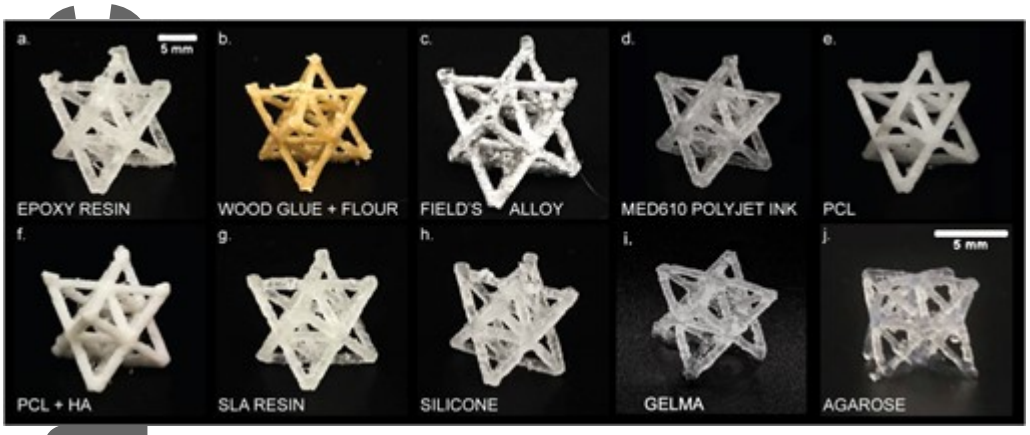


**Figure 4 | Materials versatility compatible with NEST3D printing. (A-J) Octet truss structures created using diverse classes of materials including elastomers, metals, polymers and hydrogels. Scale bar in A applicable to A-I.**

**Proliferation of osteoblastic cells NEST3D structures**

In our preliminary cytotoxicity assay described in Figure 2, we found that there were no cytotoxic leachates or residues in NEST3D printed PCL structures. To further assess the utility of NEST3D printed structures in tissue engineering, we designed a longer (2 week) experiment where a human osteoblastic cell line (MG-63) was cultured in direct contact with PCL scaffolds.[74]

NEST PCL log-pile structures of dimension 10 x 10 x 2 mm, and with measured strut diameters of 124 µm +/- 16 µm, were prepared and cleaned in the same way as in the cytotoxicity study. Osteoblastic

cells were encapsulated in 10% GelMa situated in the core of the log-pile structure (Figure 5 A). The gel was used in this way to localise the cell population so that its migration throughout the scaffold could be subsequently tracked. As a control group, we prepared cultures using same volume of cell-laden gel without the PCL NEST structure.

On day 0, both experimental groups contained the same number of initial cells. However, the NEST3D group showed increased metabolic activity over time compared to the gel only control, with a significant increase apparent by day 14 (Figure 5 D). This indicates that, at the least, the PCL structures had no detrimental effect on cell viability and that the scaffolds may even aid viability. As shown in Figure 5 D, the PCL scaffolds have highly interconnected pores with well-defined struts and alternating layers of material and open space, through which the cells would be free to migrate, giving them a proliferative advantage. Micro-CT images taken at three time points (day 0, 10 and 14) illustrate how the cell population has begun to infiltrate the PCL structure by day 14. This proliferation study further validates the suitability of the NEST3D printing process in the tissue engineering field.

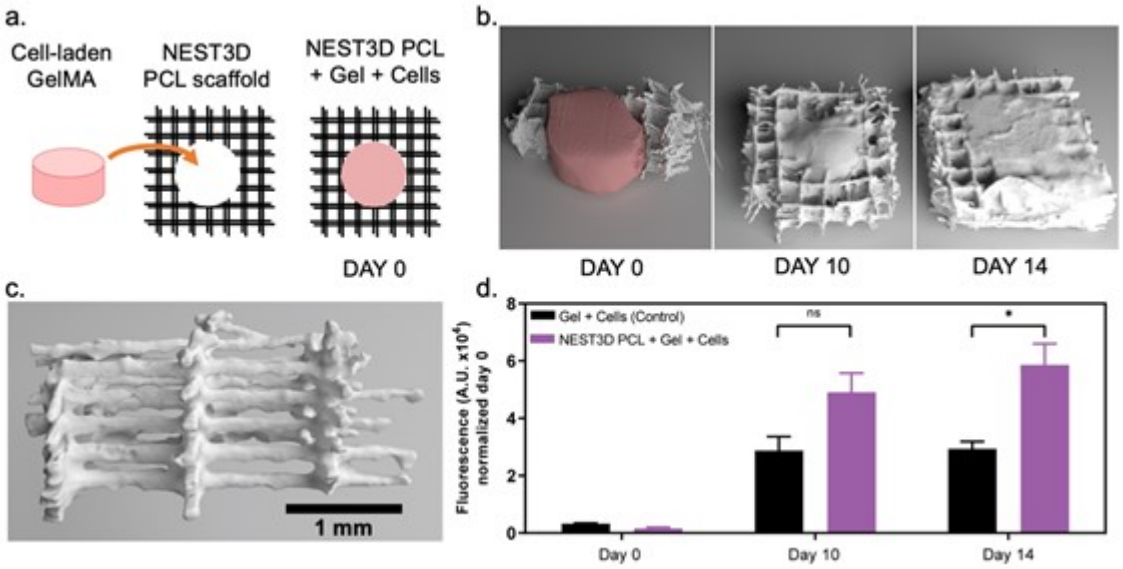


***Figure 5 | Proliferation and infiltration of osteoblastic cells in NEST3D structures.*** *(**A**) A schematic illustrating this experimental setup, where cells are encapsulated in a GelMA cylinder in the centre (core) of a PCL scaffold. The PCL scaffold has strut width of 120 µm and strut spacing of 1200 µm. (**B**) The NEST3D printed PCL scaffold facilitates cell migration through the structure by day 14. (**C**) Micro-CT rendered NEST PCL log-pile structure only showing open spaces between each layer of struts thereby allowing cells to migrate through the structure.(D) A cell viability assay showed a significant increase in the viability of a PCL NEST log-pile with osteoblastic cell-laden gel after 14 days when compared to the cell-laden gel alone.*

**Limitations of the NEST3D printing technique**

We have discussed a series of advantages afforded by NEST3D printing, especially in terms of the structural complexity and resolution of the final object, as well as the versatility of the technique across material classes. Achieving these outcomes involves several steps, and so the overall processing time must be considered: (i) *Printing the template.* Printing a NEST template of dimensions 1 x 1 x 1 cm requires approximately 2 hours at maximum resolution (0.06 mm step size).

This printing time scales with volume, so larger structures require long print times. (ii) *Casting step.* As we described above the filling time depends on the viscosity of the filling solution, the applied pressure and the dimensions of the desired structure. Casting PCL to create octet truss scaffolds shown in Figure 4 required 30 minutes. Since the flow rate scales with the radius of the struts to the fourth power (Equation 1) the filling time increases rapidly when casting finer structures. Nevertheless it is straightforward to improve average processing times in this step by casting many parts in parallel using multiple pressure chambers. (iii) *Dissolution time.* 1 $cm^3$ PVA templates can be dissolved with 5 hours of sonication in water. We expect this dissolution time to also scale with volume, although this has not yet been quantified. Again, the average processing time of this step can be easily improved by dissolving many NESTs at once.

Taken together, the time to fabricate a lattice structure with outer dimensions of approximately 1 x 1 x 1cm is about one day. Larger structures such as the tree model shown in Figure 2L required a total of one week to process. While these are relatively long timeframes to produce a single part compared to other fabrication techniques, they are comparable to the fabrication times currently required for high-value applications such as personalised biomedical implants.[75] Personalised implants can currently spend several weeks in the design and surgical planning phases, so this extra fabrication time is not expected to significantly impact on the overall lead time of a project.[76]

Another limitation of the NEST3D printing technique is the necessity (like for injection moulding) for inlet channels to fill the material. These inlet channels also fill with material and can append onto the final structure (e.g. see Figure 1H). In our latest iterations of the technique we resolve this issue in the same way as commonly done for injection moulding—by designing inlet channels which have

slight constrictions near the contact point with the part itself. When filled out, these constrictions result in weak points which can then be easily broken away after the casting and dissolution steps.

## 4. Conclusion

3D printing has become increasingly important for creating tissue engineering architectures since its introduction to the biomaterials field at the turn of the millennium.[77] While the last two decades have seen remarkable advances in applications of 3D printed biomaterials [78], current fabrication methods are still limited by the constraints of layer-by-layer deposition, materials versatility, or both.

Here, we present a novel fabrication method, Negative Embodied Sacrificial Template 3D printing, which overcomes these limitations by marrying 3D printing with injection moulding. The core advantages of NEST3D printing originate from one key observation: that our control over the 'negative space' within a 3D printed object exceeds our control over the printed material itself. Taking the widely used degradable polymer polycaprolactone as a model material, we have demonstrated how NEST3D printing readily enables "super" (sub-nozzle resolution) where a 400 µm nozzle achieves feature sizes of 140 µm thickness (vertical wall) and of 270 µm (vertical struts). We have created 3D lattice structures from PCL with a wide range of porosity (from 65% to 97%), composed of contiguous structural elements and exhibiting compressive stiffnesses that range three orders of magnitude, and in excellent agreement with FEA. Cell culture assays returned no detectable cytotoxicity of NEST3D scaffolds for hMSCs. Meanwhile, a two week culture of human osteoblastic cells within a NEST3D printed PCL scaffold confirmed the ability of these cells to proliferate and infiltrate throughout the scaffold, further validating the use of such structures in tissue engineering.

Our technique is generalizable across a plethora of materials, including biodegradable polymers, hydrogels, acrylic or epoxy resins, low-melt metal alloys, silicones and ceramics. These materials can typically be used off the shelf, without further modification. Rigorous material optimization is not required for new materials and composites to be adopted to NEST3D printing. Importantly the NEST3D printing technique requires only a consumer grade 3D printer and commonly available lab consumables, a factor that may contribute to research democratization in the additive manufacturing and tissue engineering fields. In conclusion, NEST3D printing combines an ability to produce 3D structures with complexity that rivals that achievable by light-based fabrication techniques, while also being amenable to an extraordinary range of castable materials.

## 5. Experimental Section/Methods

*Model design and preparation:* All models, unless otherwise stated, were designed in SOLIDWORKS® (Dassault Systèmes SolidWorks Corporation, Massachusetts, USA). Models were imported in STL format into Ultimaker Cura (Ultimaker, Utrecht, Netherlands) and sliced into G-code using custom settings. Custom settings of main importance are layer height: 0.06-0.2 mm (depending on application); line width: 0.4 mm; wall line count: 4; infill pattern: lines; print speed: 35mm/s; build plate adhesion: skirt; mold setting: ticked; minimal mold width: 1.2mm; support: touching build plate.

*Sacrificial template printing:* Models were printing using the Ultimaker 3 (Ultimaker, Utrecht, Netherlands). Sacrificial templates were printed with PVA (FormFutura, Nijmegen, Netherlands) using Polylactic Acid (PLA) (Ultimaker, Utrecht, Netherlands) as support material where required. BB and AA 0.4 mm print cores were used for printing sacrificial templates, but the AA print cores result

in superior definition of NEST patterns as the design mitigates PVA oozing. NEST's were typically designed with an inbuilt space that served as a reservoir for the casted material during the filling step.

*Pressure Chamber:* The pressure chamber was fabricated by casting silicone elastomer (SLYGARD™ 184 Silicone Elastomer, Dow, Michigan, USA), prepared per the manufacturer's instructions, around a 3D printed PVA insert placed inside a 30cc syringe. After curing of the PDMS, the PVA insert was removed (either manually or by via a dissolution step) to leave a cavity which matches the external dimensions of the NEST. A schematic representation can be seen in Figure S2.

Such pressure chambers based upon a 30cc syringe barrel were adequate for pressure-casting small objects with a cross-section on the order of 10 x 10 mm. For objects larger than this (such as the tree model shown in Figure 2M) we developed a 3D printed luer lock adapter to directly inject the casting material into the template from a pneumatic syringe.

*Sacrificial template filling:* The NEST was placed in the dedicated pressure chamber cavity before adding the secondary (i.e. casting) material into the template's material reservoir. The 30cc syringe is placed in a cartridge holder featuring a bayonet lock (A051-205, GESIM mbH, Radeberg, Germany) and connected to a compressor (DK50-10 S/M Mobile, Ekom, Piešťany, Slovakia) used to regulate the applied air pressure from 0-3 bar. If heat is required, the pressure chamber was placed in an oven for the duration of the filling time.

*Water treatment:* To achieve models with a smooth surface finish, NEST's were loaded into the pressure chamber as described above. The sacrificial template was then flushed through with approximately 30ml of water, and subsequently flushed with air (at 3 bar) for 10 minutes. The

sacrificial template was then placed in a dehydrator (Food Lab™ Electronic Dehydrator, Sunbeam, Florida, USA) for 10 hours at 50°C to remove excess moisture (which can cause the PVA to soften). The remainder of the filling process was continued as previously stated.

*PVA dissolution:* After the secondary material has stabilized (solidified, crosslinked, gelled, etc.), the sacrificial template is placed in water to dissolve either at 37 °C under gentle shaking (MaxQ™ 4450 Benchtop Orbital Shaker, Thermo Fisher Scientific, Massachusetts, USA) or at 4-23 °C via ultrasonication (2800 Ultrasonic Cleaner, Branson Ultrasonics Corporation, Connecticut, USA). In either case, water was replaced periodically until complete dissolution was achieved (5 hours for ultrasonication and 3-4 days under shaking).

*Modelling sacrificial template filling:* Measurements for filling rate were performed by preparing template designs incorporating individual cylindrical channels or walls which were then partially filled by applying the filling pressure for a set time. Either PCL 45,000 Mn (viscosity 1,100 Pa·s) or a low viscosity PCL blend (viscosity 110 Pa·s) were casted at 70 °C and at a pressure of 3 bar. Following template dissolution, the mass of the resulting PCL structure was measured. Each sample mass was converted to PCL volume using the density of PCL (1.145 g/cm$^3$ for 45,000 Mn PCL and the PCL blend). For each test group a technical quadruplicate (n = 4) was used.

*Rheology:* The viscosity of the PCL and low viscosity PCL blend (a 1:3 blend of 45,000 Mn and 14,000 Mn PCL) used in modelling were measured using a Physica MCR 302 Rheometer (Anton Paar, Graz, Austria) in a cone-plate geometry (15 mm diameter with a cone angle of 1°, and a truncation of 31 μm) at 70 °C and a shear rate of 1 s$^{-1}$. Shear ramp measurements showed that the viscosity of molten

PCL at 70 °C was independent of shear rate in the relevant range of 0.1 to 100 $s^{-1}$. For each test group a technical quadruplicate (n = 4) was used.

*Mechanical testing:* Compression tests were performed at room temperature using a TA Electroforce 5500 mechanical loading device (TA Instruments, Delaware, USA) fitted with a 50 lb or 250 g load cell. (Two different load cells were required owing to the large range of stiffnesses represented in the dataset). The physical dimensions of each sample (length, width, height, mass, etc.) were taken prior to testing. Samples were compressed between two stainless steel plates in an unconfined setting. The bottom plate was in a fixed position and the top plate moved following a ramp function at a rate of 0.01 mm $s^{-1}$ until a total displacement of ≈50% of the sample height or until maximum machine capabilities (200 N or 200 g). Load and displacement measurements were recorded and converted into stress (σ) and strain (ε) data using the measured cross-sectional area of the lattice unit cell and its height. The stiffness was then computed using the slope of the stress-strain curve between a strain of 0.01 and 0.03 strain. This range was chosen since it is below the yield point for PCL and represented a consistently linear region of the stress-strain curve. The elastic modulus of bulk PCL was measured in a similar manner using casted discs of dimensions 7 mm diameter, 2 mm height. For each test group a technical quadruplicate (n = 4) was used.

*Scanning Electron Microscope (SEM) Imaging:* Samples for SEM imaging were sputter coated using the EM ACE600 (Leica Microsystems, Wetzlar, Germany) to deposit 5 nm iridium. Samples were imaged using the FEI Quanta 200 SEM (Thermo Fisher Scientific, Massachusetts, USA) under high vacuum mode, 5 spot size and 30 kV accelerating voltage.

*Fourier-Transform Infrared Spectroscopy:* FTIR analysis was used to detect PVA in solution aliquots during the dissolution process. Samples undergoing the accelerated dissolution process were dissolved in 50 mL of water while samples dissolved using the passive process were placed in 50 mL phosphate buffer solution. 100% of the solution was collected and replaced at each time point. A drop of the resultant solution was added to the detection plate of the Frontier FT- IR / FIR Spectrometer with -GladiATR Accessory fitted (Perkin Elmer, Massachusetts, USA and PIKE Technologies, Wisconsin, USA). The entire spectra from 400 $cm^{-1}$ to 4000 $cm^{-1}$ was recorded with an accumulation of 8 scans per sample. Percentage transmission was read at 1270 $cm^{-1}$. For each test group a technical quadruplicate (n = 4) was used.

*Micro-CT:* Samples were imaged using the SkyScan1275 micro-CT (Bruker, Massachusetts, USA) with a source voltage of 30 kV, source current of 100 uA, image pixel size of 15 µm and 0.5˚ rotation step with no filter. No sample pre-processing was required. Reconstructed images were obtained by using the NRecon software (version 1.7.3.1, Bruker, Massachusetts, USA) with settings of: post alignment 0.50, ring artefact correction 5 and beam hardening correction 20%. Reconstructed images were then converted into a 3D structure using Materialise Mimics (Materialise, Leuven, Belgium) software and segmented to leave only the section of interest. The overlay of two 3D reconstructions was performed using Netfabb software (Autodesk, California, USA). Alternatively, reconstructed images from the proliferation study were rendered using Maya (Autodesk, California, USA).

*Finite Element Analysis (FEA) simulations:* Models for simulation were prepared using SOLIDWORKS® (Dassault Systèmes SolidWorks Corporation, Massachusetts, USA) with feature sizes (struts, walls, etc.) matching that of the physical sample. FEA analysis was performed on these models in Fusion360 (Autodesk, California, USA) by simulating their compression between two steel plates.

The elastic modulus input for PCL was 69.19 MPa as empirically measured (n = 4). Displacement and load on the top plate was recorded and converted into stress (σ) and strain (ε) data using the cross-sectional area and height. The stiffness was then computed using the slope of the stress-strain curve between a strain of 0.01 and 0.03 strain, as per the empirical measurements.

*Cytocompatibility Assay:* NEST structures (8 x 8 x 8 mm 'log-piles' with 240 µm strut diameters and 1050 µm spacing) were prepared using PCL 45 kDa and used to test cell viability with human stem cells (hMSCs). The control comparison was fresh complete cell culture medium and conditioned media from FDM PCL 45 kDa structures (GeSim BioScaffolder 3.2, GeSiM, Radeberg, Germany). hMSCs were used in conjunction with PCL log-piles prepared using the 5-hour sonication cleaning protocol, with solvent changed every hour. Primary hMSCs were isolated and cultured as previously described.[79] Once cleaned the 3D models were soaked in hMSC complete proliferation cell culture media for an additional seven days total with the conditioned media collected at 3 time points (Day 1, 3, and 7). This conditioned media was used to test cell viability on either hMSCs. Briefly, hMSCs were plated at 20,000 cells per well in a 24 well plate and cultured in complete cell culture media for 24 h before replacing with the conditioned media for an additional 24 h. CellTiter Blue (Promega, Wisconsin, USA) metabolic assay was applied following the manufacturer's instructions and incubating for 4 h at 37 °C. The surnatent was retrieved and 100 µl aliquots were places in a 96 well plate. The entire well plate was read at 550-15/600-20 emission/excitation fluorescence wavelengths using a CLARIOstar plate reader (BMG Labtech, Ortenberg, Germany). For each test group a biological quadruplicate (n = 4) was used.

*Proliferation Study:* NEST PCL log-pile structures of 120 $\mu m^3$ individual struts and overall dimension of 10 x 10 x 2 mm were prepared and cleaned in the same way as in the cytotoxicity study. Once

cleaned a 4 mm diameter biopsy punch was used to remove a cylindrical core form the centre of the log-pile. The osteoblastic cells were embedded in 10% GelMa with 0.05% LAP and the cell-laden gel was delivered to the core of the log-pile structure before crosslinking at 20 mW/cm$^2$ for 30 seconds.[80] At each time point the CellTiter Blue viability assay was performed in the same way as described in the cytotoxicity study. For each test group a biological triplicate (n = 3) was used.

*Statistical Analysis:* For each experiment and test group, four technical replicates (n = 4) were used with data summarized as the mean with error bars representing standard deviation. All statistical analysis was performed using Prism 8 (GraphPad, California, USA) with a statistical significance level ≤ 0.05. Significance for the cytocompatibility assay was determined between groups using an unpaired t test. The error associated with equations 2 and 4 is calculated by propagation of error.

*Design files:* The tree model in Figure 2L is modified from 'tree4' by TundraYeti on Thingiverse. The lattice ear in Figure 2M is modified from 'Human Ear' by addamay123 on Thingiverse. The ear scaffold was processed as a lattice using nTopology, New York, USA.

## 6. Supporting Information

Supporting Information is available from the Wiley Online Library or from the author.

## 7. Acknowledgements

**General:** The authors acknowledge the facilities, the scientific and technical assistance of RMIT University's Microscopy & Microanalysis Facility and the Vibrational Spectroscopy Facility. The

authors also acknowledge and thank Dr. Chaitali Dekiwadia from the Microscopy & Microanalysis Facility and Nadia Zakhartchouk from the Vibrational Spectroscopy Facility for their technical support. Finally, the authors acknowledge and thank Matthew Collins for his valuable assistance producing the ear lattice model.

**Funding:** This work was supported by (1) St Vincent's Hospital (Melbourne) Research Endowment Fund, (2) Victorian Medical Research Acceleration Fund (2018, Round 2), (3) NHMRC-MRFF Investigator Grant (Di Bella) #1193897 and (4) Australian Technology Network of Universities Industry Doctoral Training Centre (IDTC) scholarship.

**Author contributions:** C.D.O. conceived the idea. C.D.O., S.E.D., S.D., C.O. and E.P. designed the experiments and contributed to the data analysis and discussion of results. S.E.D. carried out all materials experimental work and simulations. S.E.D., S.D., and A.Q. carried out the cellular experimental work. C.D.O., S.E.D., S.D. and E.P. co-wrote the paper. All authors provided technical input and revised the manuscript.

**Competing interests:** The authors declare no competing interests.

**Data and materials availability:** All data needed to evaluate the conclusions in the paper are present in the paper and/or the Supplementary Materials

Received: ((will be filled in by the editorial staff))
Revised: ((will be filled in by the editorial staff))
Published online: ((will be filled in by the editorial staff))

References

[1] R. L. Truby, J. A. Lewis, *Nature* **2016**, *540*, 371.

[2] I. Kinstlinger, S. Saxton, G. Calderon, K. Ruiz, D. Yalacki, P. Deme, J. Rosenkrantz, J. Louis-Rosenberg, F. Johansson, K. Janson, D. Sazer, S. Panchavati, K.-D. Bissig, K. Stevens, J. Miller, *Nat. Biomed. Eng.* **2020**, *4*, 1.

[3] B. Grigoryan, S. J. Paulsen, D. C. Corbett, D. W. Sazer, C. L. Fortin, A. J. Zaita, P. T. Greenfield, N. J. Calafat, J. P. Gounley, A. H. Ta, F. Johansson, A. Randles, J. E. Rosenkrantz, J. D. Louis-Rosenberg, P. A. Galie, K. R. Stevens, J. S. Miller, *Science (80-. ).* **2019**, *364*, 458 LP.

[4] B. E. Kelly, I. Bhattacharya, H. Heidari, M. Shusteff, C. M. Spadaccini, H. K. Taylor, *Science (80-. ).* **2019**, *363*, 1075 LP.

[5] K. S. Lim, R. Levato, P. F. Costa, M. D. Castilho, C. R. Alcala-Orozco, K. M. A. van Dorenmalen, F. P. W. Melchels, D. Gawlitta, G. J. Hooper, J. Malda, T. B. F. Woodfield, *Biofabrication* **2018**, *10*, 34101.

[6] M. A. Skylar-Scott, J. Mueller, C. W. Visser, J. A. Lewis, *Nature* **2019**, *575*, 330.

[7] S. Gantenbein, K. Masania, W. Woigk, J. P. W. Sesseg, T. A. Tervoort, A. R. Studart, *Nat.* **2018**, *561*, 226.

[8] N. Paxton, W. Smolan, T. Böck, F. Melchels, J. Groll, T. Jungst, *Biofabrication* **2017**, *9*, 44107.

[9] M. Moini, J. Olek, J. P. Youngblood, B. Magee, P. D. Zavattieri, *Adv. Mater.* **2018**, *30*, n/a.

[10] A. Athirasala, A. Tahayeri, G. Thrivikraman, C. M. França, N. Monteiro, V. Tran, J. Ferracane, L. E. Bertassoni, *Biofabrication* **2018**, *10*, 24101.

[11] H.-W. Kang, S. J. Lee, I. K. Ko, C. Kengla, J. J. Yoo, A. Atala, *Nat. Biotechnol.* **2016**, *34*, 312.

[12] A. Lee, A. R. Hudson, D. J. Shiwarski, J. W. Tashman, T. J. Hinton, S. Yerneni, J. M. Bliley, P. G. Campbell, A. W. Feinberg, *Science (80-. ).* **2019**, *365*, 482 LP.

[13] S. Abdollahi, A. Davis, J. H. Miller, A. W. Feinberg, *PLoS One* **2018**, *13*, e0194890.

[14] Y. Zhang, L. Wu, X. Guo, S. Kane, Y. Deng, Y.-G. Jung, J.-H. Lee, J. Zhang, *J. Mater. Eng. Perform.* **2018**, *27*, 1.

[15] M. Thoury, B. Mille, T. Séverin-Fabiani, L. Robbiola, M. Réfrégiers, J.-F. Jarrige, L. Bertrand, *Nat. Commun.* **2016**, *7*, 13356.

[16] E. Chica, S. Agudelo, N. Sierra, *Renew. Energy* **2013**, *60*, 739.

[17] T. McCoy, *J. Vet. Dent.* **2014**, *31*, 126.

[18] D. Tachibana, K. Matsubara, R. Matsuda, T. Furukawa, S. Maruo, Y. Tanaka, O. Fuchiwaki, H. Ota, *Adv. Mater. Technol.* **2020**, *5*, 1900794.

[19] E. Davoodi, H. Montazerian, A. Khademhosseini, E. Toyserkani, *Acta Biomater.* **2020**, DOI https://doi.org/10.1016/j.actbio.2020.10.001.

[20] S. Mohanty, L. B. Larsen, J. Trifol, P. Szabo, H. V. R. Burri, C. Canali, M. Dufva, J. Emnéus, A.

Wolff, *Mater. Sci. Eng. C. Mater. Biol. Appl.* **2015**, *55*, 569.

[21] D. B. Kolesky, K. A. Homan, M. A. Skylar-Scott, J. A. Lewis, *Proc. Natl. Acad. Sci.* **2016**, *113*, 3179 LP.

[22] H. Zhao, W. Liang, *Mater. Lett.* **2017**, *194*, 220.

[23] H. Montazerian, M. G. A. Mohamed, M. M. Montazeri, S. Kheiri, A. S. Milani, K. Kim, M. Hoorfar, *Acta Biomater.* **2019**, *96*, 149.

[24] M. A. Woodruff, D. W. Hutmacher, *Prog. Polym. Sci.* **2010**, *35*, 1217.

[25] J. R. C. Dizon, A. D. Valino, L. R. Souza, A. H. Espera, Q. Chen, R. C. Advincula, *MRS Commun.* **2019**, *9*, 1267.

[26] L. Jiwoon, W. Jesse, N. Sanjay, Y. Sung, *Rapid Prototyp. J.* **2019**, *26*, 238.

[27] E. Sodupe Ortega, A. Sanz-Garcia, A. Pernia-Espinoza, C. Escobedo-Lucea, *Mater. (Basel, Switzerland)* **2019**, *12*, 613.

[28] D. Espinosa-Hoyos, A. Jagielska, K. Homan, H. Du, T. Busbee, D. Anderson, N. Fang, J. Lewis, K. Van Vliet, *Sci. Reports (Nature Publ. Group)* **2018**, *8*, 1.

[29] G. M. Gratson, M. Xu, J. A. Lewis, *Nature* **2004**, *428*, 386.

[30] T. D. Brown, P. D. Dalton, D. W. Hutmacher, *Adv. Mater.* **2011**, *23*, 5651.

[31] A. Bégin-Drolet, M.-A. Dussault, S. A. Fernandez, J. Larose-Dutil, R. L. Leask, C. A. Hoesli, J. Ruel, *Addit. Manuf.* **2017**, *15*, 29.

[32] S.-Z. Guo, F. Gosselin, N. Guerin, A.-M. Lanouette, M.-C. Heuzey, D. Therriault, *Small* **2013**, *9*, 4118.

[33] W. Wu, P. Geng, G. Li, D. Zhao, H. Zhang, J. Zhao, *Mater. (Basel, Switzerland)* **2015**, *8*, 5834.

[34] R. Zou, Y. Xia, S. Liu, P. Hu, W. Hou, Q. Hu, C. Shan, *Compos. B, Eng.* **2016**, *99*, 506.

[35] A. R. Torrado, D. A. Roberson, *J. Fail. Anal. Prev.* **2016**, *16*, 154.

[36] F. M. White, *Viscous Fluid Flow*, McGraw-Hill Higher Education, New York, NY, **2006**.

[37] H. Bruus, *Lab Chip* **2011**, *11*, 3742.

[38] D. Mukhtar-Fayyad, *Oral Surg. Oral Med. Oral Pathol. Oral Radiol. Endod.* **2011**, *112*, e137.

[39] P. T. Brown, A. M. Handorf, W. B. Jeon, W.-J. Li, *Curr. Pharm. Des.* **2013**, *19*, 3429.

[40] N. D. Dolinski, Z. A. Page, E. B. Callaway, F. Eisenreich, R. V Garcia, R. Chavez, D. P. Bothman, S. Hecht, F. W. Zok, C. J. Hawker, *Adv. Mater.* **2018**, *30*, 1800364.

[41] S. J. Hollister, *Nat. Mater.* **2005**, *4*, 518.

[42] X. Wang, S. Xu, S. Zhou, W. Xu, M. Leary, P. Choong, M. Qian, M. Brandt, Y. M. Xie, *Biomaterials* **2016**, *83*, 127.

[43] X. GAO, M. Fraulob, G. Haïat, *J. R. Soc. Interface* **2019**, *16*, DOI 10.1098/rsif.2019.0259.

[44] N. Shayesteh Moghaddam, M. Taheri Andani, A. Amerinatanzi, C. Haberland, S. Huff, M. Miller, M. Elahinia, D. Dean, *Biomanufacturing Rev.* **2016**, *1*, 1.

[45] B. Akhoundi, A. Behravesh, *An Int. J.* **2019**, *59*, 883.

[46] G. Domínguez-Rodríguez, J. Ku-Herrera, A. Hernández-Pérez, *Int. J. Adv. Manuf. Technol.* **2018**, *95*, 1685.

[47] J. B. Berger, H. N. G. Wadley, R. M. McMeeking, *Nature* **2017**, *543*, 533.

[48] X. Zheng, H. Lee, T. H. Weisgraber, M. Shusteff, J. DeOtte, E. B. Duoss, J. D. Kuntz, M. M. Biener, Q. Ge, J. A. Jackson, S. O. Kucheyev, N. X. Fang, C. M. Spadaccini, *Science (80-. ).* **2014**, *344*, 1373 LP.

[49] A. Nazir, K. Abate, A. Kumar, J.-Y. Jeng, *Int. J. Adv. Manuf. Technol.* **2019**, *104*, 3489.

[50] M. Mohsenizadeh, F. Gasbarri, M. Munther, A. Beheshti, K. Davami, *Mater. Des.* **2018**, *139*, 521.

[51] W. Chen, X. Zheng, S. Liu, *Mater. (Basel, Switzerland)* **2018**, *11*, 2073.

[52] C. Bader, N. Oxman, *Comput. Des.* **2016**, *81*, 39.

[53] S. Eshraghi, S. Das, *Acta Biomater.* **2010**, *6*, 2467.

[54] C.-H. Chen, V. B.-H. Shyu, J.-P. Chen, M.-Y. Lee, *Biofabrication* **2014**, *6*, 15004.

[55] W. Y. Yeong, N. Sudarmadji, H. Y. Yu, C. K. Chua, K. F. Leong, S. S. Venkatraman, Y. C. F. Boey, L. P. Tan, *Acta Biomater.* **2010**, *6*, 2028.

[56] J. M. Williams, A. Adewunmi, R. M. Schek, C. L. Flanagan, P. H. Krebsbach, S. E. Feinberg, S. J. Hollister, S. Das, *Biomaterials* **2005**, *26*, 4817.

[57] A. D. Olubamiji, Z. Izadifar, J. L. Si, D. M. L. Cooper, B. F. Eames, D. X. B. Chen, *Biofabrication*

**2016**, *8*, 25020.

[58] D. W. Hutmacher, T. Schantz, I. Zein, K. W. Ng, S. H. Teoh, K. C. Tan, *J. Biomed. Mater. Res.* **2001**, *55*, 203.

[59] S. A. Park, S. H. Lee, W. D. Kim, *Bioprocess Biosyst. Eng.* **2011**, *34*, 505.

[60] W. F., S. L., D. A., K. S., S. W., G. S., L. A., *Rapid Prototyp. J.* **2004**, *10*, 42.

[61] J. Visser, F. P. W. Melchels, J. E. Jeon, E. M. van Bussel, L. S. Kimpton, H. M. Byrne, W. J. A. Dhert, P. D. Dalton, D. W. Hutmacher, J. Malda, *Nat. Commun.* **2015**, *6*, 6933.

[62] K. J. McHugh, T. D. Nguyen, A. R. Linehan, D. Yang, A. M. Behrens, S. Rose, Z. L. Tochka, S. Y. Tzeng, J. J. Norman, A. C. Anselmo, X. Xu, S. Tomasic, M. A. Taylor, J. Lu, R. Guarecuco, R. Langer, A. Jaklenec, *Science (80-. ).* **2017**, *357*, 1138 LP.

[63] F. Gilbert, C. D. O'Connell, T. Mladenovska, S. Dodds, *Sci. Eng. Ethics* **2018**, *24*, 73.

[64] Ż. Górecka, J. Idaszek, D. Kołbuk, E. Choińska, A. Chlanda, W. Święszkowski, *Mater. Sci. Eng. C* **2020**, *114*, 111072.

[65] A. A. Soufivand, N. Abolfathi, A. Hashemi, S. J. Lee, *Polym. Adv. Technol.* **2020**, *31*, 1038.

[66] U. Ripamonti, *Biomaterials* **1996**, *17*, 31.

[67] Ultimaker, *Technical Data Sheet PVA*, **2017**.

[68] S. K. Saxena, *POLYVINYL ALCOHOL (PVA)*, **2004**.

[69] Sigma-Aldrich, **2013**.

[70] S. Caba, M. Koch, *AIP Conf. Proc.* **2016**, *1779*, 70002.

[71] T. Moritz, S. Maleksaeedi, in (Eds.: J. Zhang, Y.-G.B.T.-A.M. Jung), Butterworth-Heinemann, **2018**, pp. 105–161.

[72] A. Lipchitz, G. Harvel, T. Sunagawa, *EXPERIMENTAL INVESTIGATION OF THE THERMAL CONDUCTIVITY AND VISCOSITY OF LIQUID In-Bi-Sn EUTECTIC ALLOY (FIELD'S METAL) FOR USE IN A NATURAL CIRCULATION EXPERIMENTAL LOOP*, **2015**.

[73] E. Fernández, D. López, C. Mijangos, M. Duskova-Smrckova, M. Ilavsky, K. Dusek, *J. Polym. Sci. Part B Polym. Phys.* **2008**, *46*, 322.

[74] S. Staehlke, H. Rebl, B. Nebe, *Cell Biol. Int.* **2019**, *43*, 22.

[75] A. Koptyug, L.-E. Rännar, M. Bäckström, S. Fager Franzén, P. Dérand, *Int. J. Life Sci. Med. Res.* **2013**, *3*, 15.

[76] K. Willemsen, R. Nizak, H. J. Noordmans, R. M. Castelein, H. Weinans, M. C. Kruyt, *Lancet Digit. Heal.* **2019**, *1*, e163.

[77] D. W. Hutmacher, *Biomaterials* **2000**, *21*, 2529.

[78] A. C. Daly, G. M. Cunniffe, B. N. Sathy, O. Jeon, E. Alsberg, D. J. Kelly, *Adv. Healthc. Mater.* **2016**, *5*, 2353.

[79] G. Onofrillo, S. Duchi, C. D. O'Connell, R. Blanchard, A. J. O'Connor, M. Scott, G. G. Wallace, P. F. M. Choong, C. Di Bella, *Biofabrication* **2018**, *10*, 45006.

[80] C. Onofrillo, S. Duchi, S. Francis, C. D. O'Connell, L. M. Caballero Aguilar, S. Doyle, Z. Yue, G. G.

Wallace, P. F. Choong, C. Di Bella, *Biomaterials* **2021**, *264*, 120383.

[81] Lebel, L.L., Aissa, B., Khakani, M.A.E. and Therriault, D., 2010. *Advanced Materials,* 22(5), pp.592-596.

[82] J. S. Miller, K. R. Stevens, M. T. Yang, B. M. Baker, D.-H. T. Nguyen, D. M. Cohen, E. Toro, A. a Chen, P. a Galie, X. Yu, R. Chaturvedi, S. N. Bhatia, C. S. Chen, Nat. Mater. 2012, 11, 1.

[83] M. K. Gelber, G. Hurst, T. J. Comi, R. Bhargava, Addit. Manuf. 2018, 22, 38.

[84] F. Gilbert, C. D. O'Connell, T. Mladenovska, S. Dodds, Sci. Eng. Ethics 2017, DOI 10.1007/s11948-017-9874-6.

**Table of contents (ToC) entry**

Through our new technique termed Negative Embodied Sacrificial Template 3D (NEST3D) printing we demonstrate how the negative pattern within a 3D printed object can describe geometries and microarchitectures that are not possible to extrusion print directly, at definitively higher resolution and by casting in a secondary material the technique is amendable to a plethora of materials.

*Stephanie E. Doyle, Serena Duchi, Carmine Onofrillo, Anita Quigley, Claudia Di Bella, Elena Pirogova, Cathal D. O'Connell*[*]

Printing between the lines: Intricate biomaterial structures fabricated via Negative Embodied Sacrificial Template 3D (NEST3D) Printing

**ToC figure** ((Please choose one size: 55 mm broad × 50 mm high **or** 110 mm broad × 20 mm high. Please do not use any other dimensions))